Experimental Mechanics
DOI 10.1007/s11340-009-9299-5

Local Strain Concentrations in a Microvascular Network

A.R. Hamilton · N.R. Sottos · S.R. White

Received: 18 November 2008 / Accepted: 18 September 2009

Abstract Strain concentrations associated with the presence of a microvascular network in a polymer matrix are measured using fluorescent digital image correlation (FDIC). The accuracy of the measurement technique is established for a specimen containing only a single microchannel. The influence of localized particle reinforcement around the channel is also investigated using this simplified geometry. Three-dimensional network specimens with different structural designs were fabricated and loaded in uniaxial tension. The resulting strain concentrations are compared as a function of channel spacing and location. As expected, decreasing channel spacing leads to increased strain local to the channels. In addition, the three-dimensional nature of the channel architecture influences the resulting strain. The results provide insight into the mechanical behavior of microvascular networks and demonstrate the utility of FDIC as a characterization tool at these length scales.

Keywords Digital image correlation · Self-healing · Microvascular · Microchannels · Biomimetic

Introduction

Living organisms rely on pervasive vascular systems to deliver, circulate, and remove chemical agents for such critical biological functions as tissue growth and repair, temperature regulation, and defense against disease. While circulatory networks are most often associated with soft tissue, there are also numerous examples in nature of circulatory networks in structural, hard tissue.

Human cortical bone is a vascularized, structural material with a complex hierarchical organization that results in substantial strength and toughness. The distribution of mechanical properties around the Haversian canals lowers the stress concentration and redistributes load away from the defects introduced by the vasculature [1]. This architecture reduces the influence of the Haversian canals on the behavior of an advancing crack, leaving other toughening mechanisms (mostly crack bridging) to dominate the fracture toughness [2, 3]. Dentin, which makes up the bulk of human teeth below the enamel layer, has a microstructure consisting of tubules 1 to 2 μm in diameter that are reinforced by a higher concentration of a stiff mineral phase. The ratio of the elastic moduli of this reinforced (peritubular) dentin to the bulk (intertubular) dentin has been estimated between 1.7 and 2.9, with the thickness of the peritubular material around 0.5 to 0.8 μm [4]. In contrast to bone, this distribution of mechanical properties in dentin gives rise to microcracking between the mineral-reinforced tubules (depicted in Fig. 1)—one of the extrinsic toughening mechanisms observed in dentin [5].

Advances in soft lithographic and direct-write assembly methods have enabled the creation of synthetic materials with complex embedded microvascular networks that emulate many of the key responses of biological vascular systems [6–10]. Toohey et al. have reported a self-healing coating/substrate design [7, 11] that delivers healing agent to cracks in a coating via

A.R. Hamilton (SEM member) · N.R. Sottos (✉, SEM member) · S.R. White (SEM member)
University of Illinois at Urbana-Champaign,
Urbana, IL, USA
e-mail: n-sottos@illinois.edu

Published online: 10 November 2009

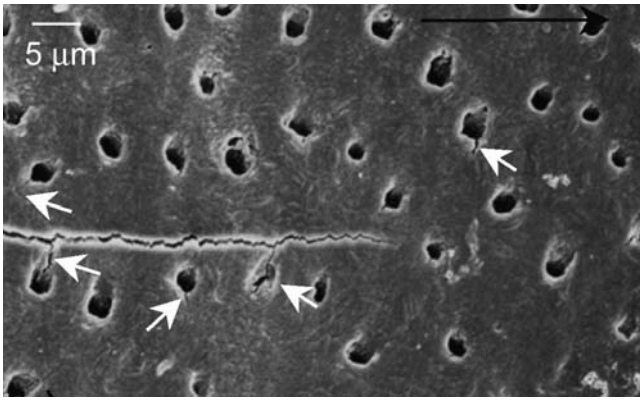

Fig. 1 Crack propagation through dentin, with microcracking highlighted by *arrows*. Reprinted from [3] with permission from Elsevier

a three-dimensional microvascular network in the substrate. Williams et al. [12, 13] have developed a vascularized composite sandwich structure that is capable of rebonding impact-induced delamination damage. The continuous delivery of healing components through a vascular network represents a significant advance over previously reported self-healing materials in which a finite supply of healing agent is stored in capsules or hollow fibers [14–18]. In contrast to these compartmentalized approaches, vascularized systems distribute healing agent throughout the material, such that any given part has access to the supply of the whole system. Recent analyses suggest ways to design and optimize these vascularized networks for healing and cooling with minimized impact on structural performance [19–22]. In order to realize these optimized structures, the mechanical integrity of the network must be characterized.

In the current work, we explore the effects of channel spacing and channel reinforcement on the local strain concentrations in a microvascular self-healing composite. Displacement and strain are measured by a fluorescent digital image correlation (FDIC) technique [23, 24] in samples with a 0–90° stacking sequence between layers of microchannels. This geometry was implemented for the healing of cracks in brittle coatings by Toohey et al. [7]. The experimental technique is first verified on a finite strip with an isolated microchannel loaded in tension, for which an analytical solution exists. Measurements on fully three-dimensional networks reveal the influence of channel spacing on the mechanical behavior.

Sample Preparation

Single-channel samples were produced by threading nylon wire (280 μm in diameter) across a rubber mold into which a two-part epoxy was poured and allowed to cure. The nylon wire was removed and, after cutting and polishing, the resulting sample was a thin rectangular strip with a centrally positioned, isolated microchannel running through the thickness. The epoxy matrix used in all samples was Epon 828 resin (DGEBA) and Epikure 3274 curing agent (blend of polyoxyalkyleneamine and nonyl phenol).

In some single-channel specimens, the channel was locally reinforced by silane-functionalized 9.5 μm alumina particles. The particle reinforcement was incorporated by deposition onto a wax scaffold created via the direct-write fabrication technique [6]. After infiltration of the polymer matrix and removal of the wax ink, the particles remained embedded in the material surrounding a 200 μm diameter microchannel. Figure 2(a)

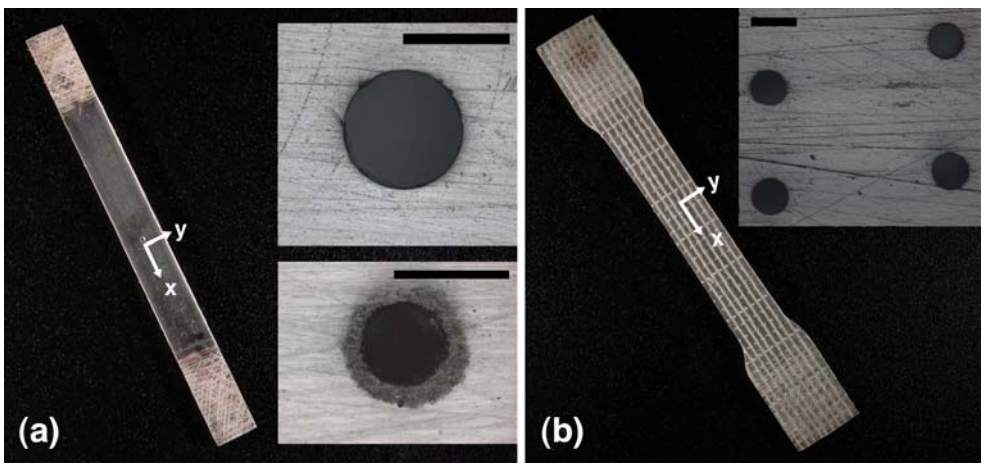

Fig. 2 Images of (**a**) single channel samples with micrographs of both unreinforced (*top*) and reinforced (*bottom*) channels and (**b**) a representative microvascular network sample with a micrograph of channel layout. *Scalebars* are 250 μm

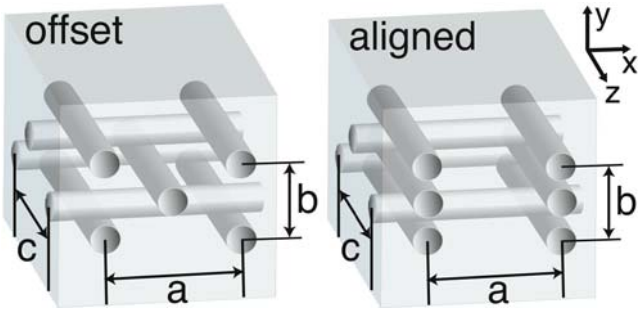

Fig. 3 Schematic drawings and nomenclature for different microvascular network sample geometries

depicts a single channel sample with micrographs of both an unreinforced and reinforced microchannel.

Epoxy matrix samples containing microvascular networks were manufactured by direct-write fabrication described previously by Toohey et al. [7] and Therriault et al. [6]. A fugitive organic ink (60% microcrystalline wax, 40% petroleum jelly by weight) was deposited in a layer-by-layer manner with depositions placed at every location where a microchannel was desired in the final sample. The resulting ink scaffold was then infiltrated with liquid epoxy and allowed to cure. The ink was subsequently removed by moderate heating (80°C) and applying vacuum to the microchannel outlets.

The resulting samples contained embedded microvascular networks of 200 μm diameter channels that were fully connected in three dimensions. The samples had a 0–90° stacking sequence between subsequent layers of channels, with connections from one layer to the next at the channel intersections. Figure 2(b) is a representative image of a microvascular sample, with a micrograph inset revealing the microchannel cross-section. As detailed in Fig. 3 and Table 1, three different microvascular geometries (denoted I, II, III) were created for testing by varying the spacing between channels in the *xy* plane. Channel spacing in the *yz* plane was the same among all microvascular sample geometries. Small deviations in the relative position of microchannels on the order of a few microns were common due to imperfections in the manufacturing process.

Table 1 Sample geometry dimensions

Label	Architecture	a (mm)	b (mm)	c (mm)
Type I	Offset	2.0	0.7	2.0
Type II	Offset	1.0	0.7	2.0
Type III	Aligned	2.0	0.7	2.0

Experimental Procedure

Fluorescent Digital Image Correlation

Fluorescent digital image correlation (FDIC) is a full-field technique for measuring strain and displacement. As in digital image correlation [25, 26], a correlation algorithm is applied to obtain kinematic information from digital images acquired during deformation. The correlation requires random surface features that deform with the specimen surface; in FDIC this pattern is created by applying fluorescent silica nanoparticles onto the region of interest. The fluorescent particles create a much smaller and finer surface pattern than paint. This fine pattern makes the correlation of high magnification images possible. In work done by Berfield et al. with 180 nm fluorescent particles, a displacement resolution of 20 nm was reported [23, 24].

For the current investigation, particles with a mean diameter of approximately 380 nm created an appropriate surface pattern for the optical setup and the feature size of interest. A typical surface pattern resulting from the application of these fluorescent nanoparticles is shown in Fig. 4. The particles do not have any significant impact on the mechanical behavior of the sample because they are disperse and small relative to the sample thicknesses, which were all greater than 1 mm. Particles containing the fluorescent dye rhodamine B were synthesized following the procedure described by Verhaegh et al. [27].

The optical system for acquisition of FDIC images consisted of a Leica DMR fluorescent microscope, a

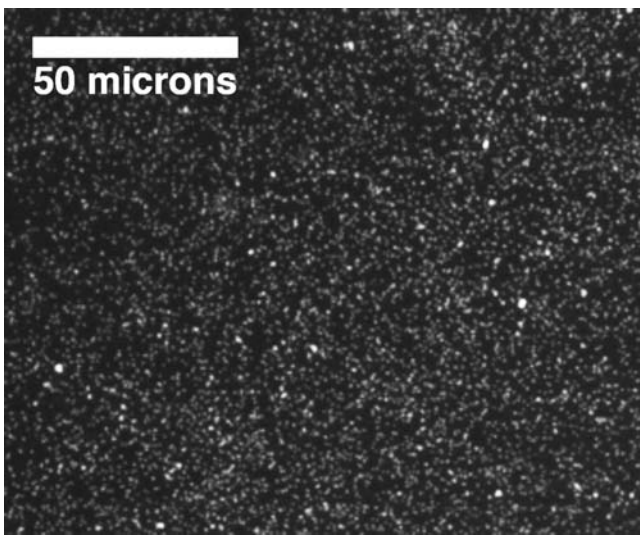

Fig. 4 Representative speckle pattern formed by deposition of fluorescent nanoparticles onto a sample surface

20× magnification Leica long working distance objective lens (0.4 N.A. and 3.5 μm depth of focus), and a QCapture Retiga CCD camera. With a pixel density of 1.88 pixels/μm, this setup has a resolving power of 826 nm based on the Rayleigh criterion for self-luminescent objects. Using this setup, calibration experiments verified a displacement resolution of approximately 20 nm for rigid body translations, similar to that reported by Berfield et al. [23]. However, when the technique is applied in the presence of a heterogeneous strain field the displacement resolution may be affected. [28]

Correlations were performed using an in-house DIC code in which a coarse–fine search is implemented to obtain an initial guess for a Newton–Raphson scheme [25]. More recent finite-element based DIC algorithms that easily interface with computational modeling [29] could also be used to analyze the displacement and strain, but were not implemented for this work. Subset sizes were 31 by 31 pixels (16.5 μm), and correlations were performed every 10 pixels (5.3 μm). Correlation was not attempted anywhere inside the channel boundary, where the displacement becomes discontinuous. Accordingly, no displacement and strain data were obtained within a distance approximately the size of a subset around each channel. Strain was calculated by numerically differentiating the displacement measured by DIC, rather than using the displacement gradients obtained from the correlation directly. Displacement data were smoothed using a moving average that was computed as the arithmetic mean of the displacement at a point and the eight adjacent points. Displacement gradients were calculated using a finite-difference scheme. Wherever possible, a four-point central difference technique was used to compute the displacement gradients. Lower-order central, forward, and backward difference techniques were substituted where boundaries prevented the use of four-point central difference. Strain data computed using these finite-difference schemes were in good agreement with the strain data obtained from the DIC algorithm directly, but contained less noise.

Test Protocol

Samples were loaded in tension along the x axis (according to the coordinate system established in Fig. 3) using a miniature load frame (Ernest F. Fullam, Inc.) while viewing the xy plane of the sample. The applied load was measured using a 100 lb capacity load cell (Entran). Samples were clamped tightly in flat-faced grips and loaded at a rate of 1 μm/s. Deformation was paused at regular intervals to capture fluorescent images for correlation. A dual-axis translation stage mounted to the microscope was used to minimize rigid body translations during loading. Out-of-plane movements and Poisson effects required refocusing the optical setup after application of load, but refocusing was not found to have a significant effect on results. Load data were used to calculate the far-field values of strain, $\epsilon_o = \sigma/E$. The elastic modulus of the epoxy matrix was 3.35 ± 0.15 GPa for the range of samples tested. Dynamic mechanical analysis of the matrix material was performed to establish these values of modulus.

Results and Discussion

Single Channel Specimen

The experimentally determined displacement and strain fields in the loading (x) direction around an isolated microchannel—280 μm in diameter—under uniaxial tension are shown in Fig. 5. Contours are drawn at 50 nm intervals over a total range of displacement of 3.8 μm. The iso-displacement contours, which without the presence of the channel would be vertically oriented

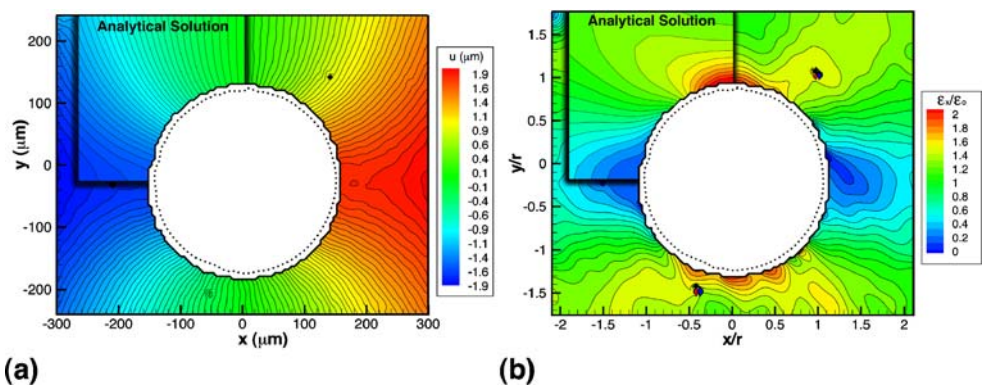

Fig. 5 Experimentally determined (**a**) displacement and (**b**) strain fields in the vicinity of an isolated 280 μm diameter microchannel with analytical solution inset on upper left for comparison. $\epsilon_o = 0.39\%$

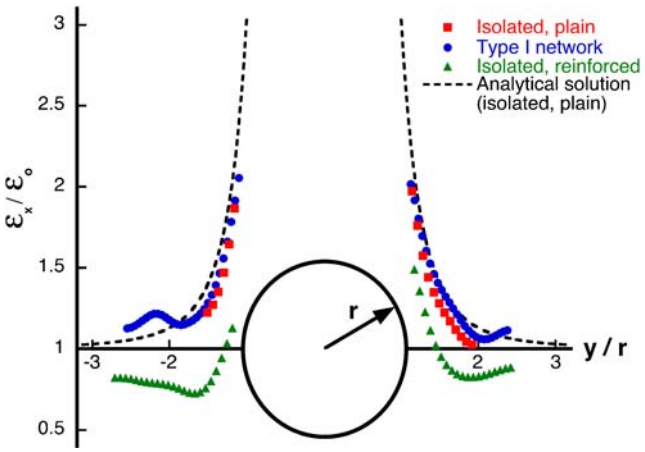

Fig. 6 Normalized strain along a vertical line through the center of each corresponding microchannel

and straight, curve into the channel. As expected, a strain concentration develops at the top $(+y)$ and bottom $(-y)$ of the microchannel, while the strain drops almost to zero on the left $(-x)$ and right $(+x)$ sides.

An analytical solution for a finite-width plate in uniaxial tension [30] is inset on the upper left corners of the contour plots in Fig. 5(a) and (b). Experimentally-determined strain and displacement are in excellent agreement with this analytical solution. The normalized strain along a vertical line through the center of the channel is plotted in Fig. 6. This plot shows the maximum observed strain concentration was 1.9, while the value predicted by the analytical solution is 3.0. This difference is due to the limited spatial resolution of FDIC, which is approximately equal to the subset size used in the correlation. Furthermore, the strain concentration is greatest at the boundary of the channel, but correlations were not performed directly adjacent to this boundary.

Microvascular Network Specimens

A full microvascular network adds the complexity of a periodic array of microchannels positioned throughout the matrix in three dimensions. In addition to the channels normal to the xy plane, all microvascular samples had channels normal to the yz plane that are not visible on the surface imaged for DIC. Due to the staggered channel layout in the yz plane, every other subsurface microchannel was offset by 1 mm in the z direction.

The type I network geometry had the largest spacing between neighboring microchannels in the xy plane. The normalized strain field around a single microchannel in this type I geometry is shown in Fig. 7(a). The shape of the strain contours is similar to those surrounding a single, isolated microchannel. As shown in Fig. 6, the maximum normalized strain is slightly higher for this network sample (2.1) than for the single channel sample (1.9), and the strain concentration remains higher farther from the microchannel. The highest strain concentration in the network specimen occurs on the bottom $(-y)$ side of the microchannel, where a subsurface microchannel is located closer to the surface. The strain concentration on the top $(+y)$ side of the microchannel is approximately the same as the strain concentration in the single-microchannel sample.

The strain field between two microchannels in a type I microvascular geometry is shown in Fig. 7(b). Interestingly, the strain falls to approximately far-field levels directly between the two microchannels, but remains elevated along bands to the left and right of the microchannels. Again, a higher strain concentration occurs where the closer subsurface microchannel intersects a channel normal to the xy plane (above the bottom microchannel, near $y/r = -2.1$ and $x/r = 0$). The normalized strain along a line connecting the centers of these two microchannels is plotted in Fig. 8.

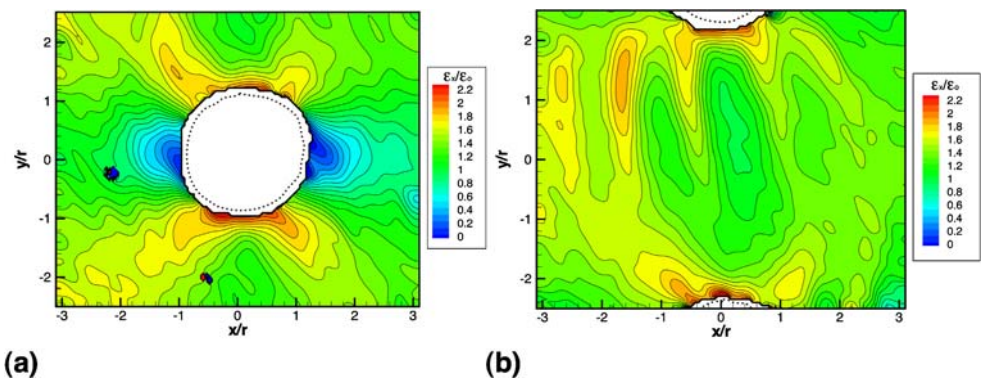

Fig. 7 Experimentally determined strain fields (**a**) surrounding and (**b**) between 200 μm diameter microchannels in a type I microvascular network sample. $\epsilon_o = 0.18\%$ and 0.32%, respectively

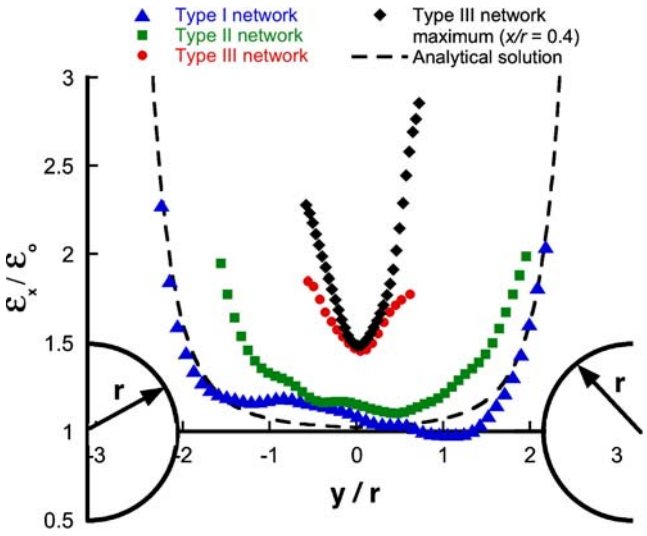

Fig. 8 Normalized strain along a line connecting the centers of two microchannels in each of the network geometries

For comparison, the analytical solution for a single, isolated channel is also plotted at each microchannel location. The strain around each of these two microchannels is comparable with that of the solution for an isolated channel, with the exception of the bottom half of the strain field $(-y)$ where the strain in the network remains above the far-field value away from the microchannel. This region of elevated strain is associated with the microchannel that intersects the nearest subsurface channel.

There are other factors, in addition to the subsurface channels, that may influence the mechanical response of a network specimen, which are not present in a single-channel sample. The periodic arrangement of microchannels normal to the xy plane could contribute to differences in the strain fields. Also, the microchannel cross-sections are not perfectly round due to deformation of the wax ink during processing. Despite these effects, the strain field that develops in this type I network sample is remarkably similar to that of a single-microchannel sample.

In the type II microvascular geometry, the distance between microchannels in the x direction was closer than in a type I sample. The normalized strain field surrounding three microchannels is shown in Fig. 9(a) for a type II network sample. As in the type I network, the maximum strain concentration in the type II network (2.3) occurs at the microchannel that is intersected by the nearest subsurface microchannel (the bottom left microchannel, near $y/r = -1.5$ and $x/r = -2$). Although the maximum strain concentration is about the same as in the type I sample, the closer x-direction spacing confines the region of elevated strain. This confining occurs because the strain must drop to a minimum at the left side of the neighboring microchannel over a shorter distance than in a type I sample. The strain plotted in Fig. 8 for a type II network reveals a trend similar to that in the type I network. However, the strain in the type II network does not drop to the same minimum strain seen in the analytical solution far from the channel. Note that maximum strain concentration in Fig. 9(a) is not plotted in Fig. 8, because the maximum occurs off center from the two microchannels.

The type III microvascular geometry had neighboring microchannels that are in the closest proximity to one another, because there was no offset between subsequent layers in the y-direction. Because the y spacing was less in this geometry, the locations of maximum strain concentration (the tops and bottoms of microchannels) have the least separation in these samples. Consequently, the normalized strain field in Fig. 9(b) shows higher levels of strain concentration (up to 2.8) at locations farther from the microchannels than in the previous two network geometries. The location of the maximum strain concentration is off-center on

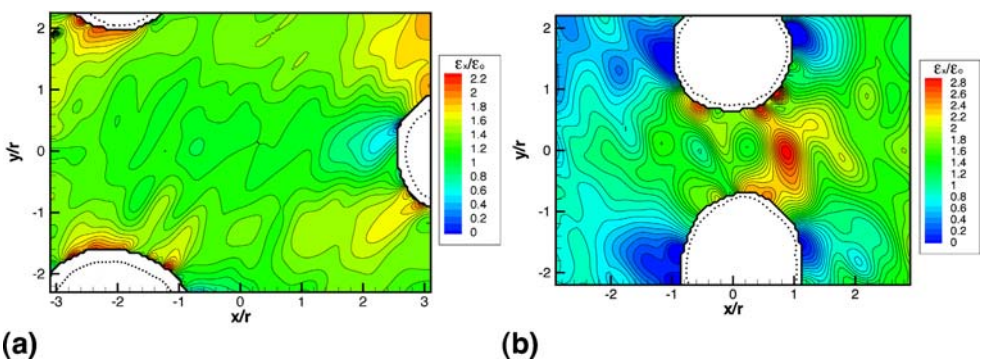

Fig. 9 Experimentally determined strain fields between 200 μm diameter microchannels in (**a**) type II and (**b**) type III microvascular network samples. $\epsilon_o = 0.15\%$ and 0.05%, respectively

the right ($+x$) side of the microchannels. This shift in location of the maximum strain is probably due to an asymmetry at the intersection between the subsurface microchannel with the microchannels normal to the xy plane. There are two line scans plotted in Fig. 8 for the type III geometry; one of them is a plot of the strain between the centers of the two channels ($x/r = 0$). The other is a plot of the strain along a vertical line through the region of maximum strain ($x/r = 0.4$). The strain along both of these vertical lines remains well above the level of strain far from the channels in all the previous geometries and in the analytical solution.

Reinforced Single Channel Specimen

The stiffening effect of particle reinforcement locally placed around a single 200 μm diameter microchannel is evident from the normalized strain field in Fig. 10. The strain around a reinforced channel drops to values at or below the far-field strain in a shorter distance from the channel as compared with the case of the unreinforced channel in Fig. 6. Because the reinforced material surrounding the channel is stiffer than the matrix, there is a decrease in strain when approaching this region. The asymmetry of the strain concentration is due to the uneven distribution of the reinforcement around the channel. The ring of particle reinforcement was thinnest on the top ($+y$) side of the channel, where the strain concentration is highest (1.6).

The Young's modulus of the reinforced region was estimated by comparing the experimentally determined displacement field with an analytical solution for a circular hole reinforced with an elastic ring in an infinite plate [31]. This comparison is made in Fig. 11 using a Young's modulus of 11.5 GPa for a 45 μm thick reinforced region. The analytical model assumes that the interface between the two materials is perfect, resulting in a sharp change in curvature of the analytical iso-displacement contours at the interface. The experimental iso-displacement contours are smoother, both because the interface of the real sample is inevitably graded to some degree, and because of the limited spatial resolution of the experimental technique.

The thickness of the reinforced region for the analytical solution was estimated from a transmission light micrograph of the reinforced microchannel. The Young's modulus of the reinforced region was estimated using a model for particle composites developed by Paul [32]

$$E_c = E_m \frac{1 + (m-1)V_p^{2/3}}{1 + (m-1)(V_p^{2/3} - V_p)} \tag{1}$$

where E_c and E_m are the Young's modulus of the composite and matrix, m is the ratio of the Young's modulus of the particulate to that of the matrix, and V_p is the volume fraction of particle reinforcement. The Young's modulus of the epoxy matrix and alumina particles was taken as 3.2 GPa and 300 GPa respectively, and the volume fraction of reinforcement used was 40%. This volume fraction was selected to obtain the best agreement between the analytical solution and measured displacement field in Fig. 11, but we obtained a similar volume fraction of particles (43%) by measuring the area fraction of particles in a micrograph of the reinforced channel. Interestingly, the ratio of the reinforced region's elastic modulus to that of the matrix

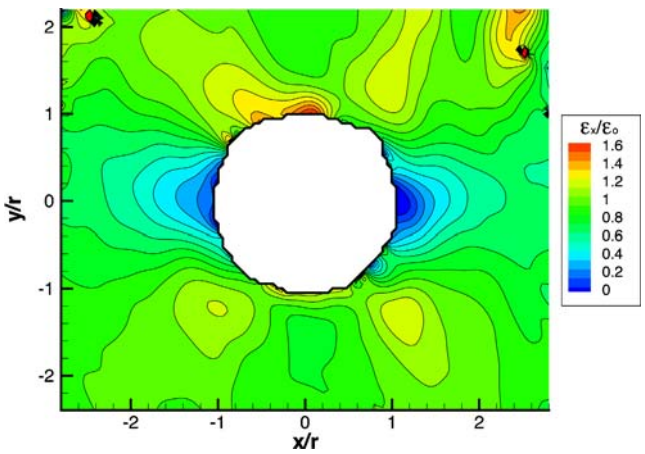

Fig. 10 Experimentally determined strain field around an isolated 200 μm diameter reinforced channel. $\epsilon_o = 0.44\%$

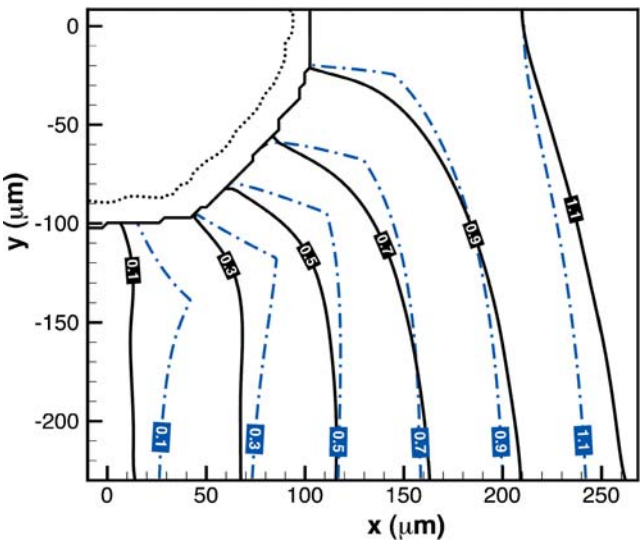

Fig. 11 Experimentally determined (*solid*) and analytically predicted (*dashed*) displacement fields around a 200 μm diameter reinforced channel

is 3.6, similar to that of the elastic moduli of peritubular and intertubular dentin.

Conclusions

Measurements of the displacement field surrounding a single channel in tension were made and verified with an analytical solution. Excellent agreement was obtained between experimental and analytical displacement and strain fields, demonstrating the ability of fluorescent DIC to make accurate measurements of the mechanical response around a microchannel. Samples with a fully three-dimensional microvascular network had higher strain concentrations compared with that caused by a single, isolated microchannel. These higher strain concentrations are attributed to the influence of subsurface microchannels, microchannel cross-sectional shape, and neighboring microchannels. Inter-channel spacing in the direction perpendicular to the loading direction had the largest impact on the magnitude of strain concentration.

Localized particle reinforcement significantly altered the strain concentration around the microchannels. In addition to increasing the local stiffness of a microvascular network, local reinforcement may enable the mimicry of such biological systems as dentin. In the presence of an advancing crack, the microvascular network geometry and the distribution of mechanical properties of the matrix will influence crack propagation and the bulk material response. Processing methods are under development for selectively reinforcing channels in three-dimensional microvascular networks.

Overall, the measurement of strain fields using fluorescent digital image correlation should provide valuable insight into the design of microvascular networks, and aid in achieving effective self-healing while maintaining optimal structural performance.

Acknowledgement This work was supported by the Air Force Office of Scientific Research Multidisciplinary University Research Initiative (grant F49550-05-1-0346).

References

1. Gotzen N (2003) Understanding stress concentration about a nutrient foramen. J Biomech 36:1511–1521
2. Nalla R, Kinney J, Ritchie R (2003) Mechanistic fracture criteria for the failure of human cortical bone. Nat Mater 2:164–168
3. Nalla R, Kruzic J, Ritchie R (2004) On the origin of the toughness of mineralized tissue: microcracking or crack bridging? Bone 34:790–798
4. Balooch G, Marshall G, Marshall S, Warren O, Asif S, Balooch M (2004) Evaluation of a new modulus mapping technique to investigate microstructural features of human teeth. J Biomech 37:1223–1232
5. Nalla R, Kinney J, Ritchie R (2003) Effect of orientation on the *in vitro* fracture toughness of dentin: the role of toughening mechanisms. Biomaterials 24:3955–3968
6. Therriault D, White S, Lewis J (2003) Chaotic mixing in three-dimensional microvascular networks fabricated by direct-write assembly. Nat Mater 2:265–271
7. Toohey K, Sottos N, Lewis J, Moore JS, White S (2007) Self-healing materials with microvascular networks. Nat Mater 6:581–585
8. Runyon M, Johnson-Kerner B, Ismagilov R (2004) Minimal functional model of hemostasis in a biomimetic microfluidic system. Angew Chem, Int Ed 43:1531–1536
9. Stroock A, Cabodi M (2006) Microfluidic biomaterials. MRS Bull 31:114–119
10. Lim D, Kamotani Y, Cho B, Mazumder J, Takayama S (2003) Fabrication of microfluidic mixers and artificial vasculatures using a high-brightness diode-pumped nd : Yag laser direct write method. Lab Chip 3:318–323
11. Toohey K, Sottos N, Lewis J, Moore JS, White S (2009) Characterization of microvascular-based self-healing coatings. Exp Mech 49(5):707–717
12. Williams HR, Trask RS, Bond IP (2007) Self-healing composite sandwich structures. Smart Mater. Struct. 16:1198–1207
13. Williams HR, Trask RS, Bond IP (2008) Self-healing sandwich panels: restoration of compressive strength after impact. Compos Sci Technol 68:3171–3177
14. White S, Sottos N, Geubelle P, Moore J (2001) Autonomic healing of polymer composites. Nature 409:794–797
15. Keller MW, White SR, Sottos NR (2007) A self-healing poly(dimethyl siloxane) elastomer. Adv. Funct. Mater. 17:2399–2404
16. Caruso MM, Blaiszik BJ, White SR, Sottos NR, Moore JS (2008) Full recovery of fracture toughness using a nontoxic solventbased selfhealing system. Adv. Funct. Mater. 18:1898–1904
17. Pang J, Bond I (2005) A hollow fibre reinforced polymer composite encompassing self-healing and enhanced damage visibility. Compos Sci Technol 65:1791–1799
18. Brown E, Sottos N, White S (2002) Fracture testing of a self-healing polymer composite. Exp Mech 42:74–83
19. Aragón A, Hansen C, Wu W, Geubelle P, Lewis J (2007) Computational design and optimization of a biomimetic self-healing/cooling composite material. Proc SPIE 6526: 1G1–1G10
20. Kim S, Lorente S, Bejan A (2006) Vascularized materials: tree-shaped flow architectures matched canopy to canopy. J Appl Phys 100:063525
21. Williams HR, Trask RS, Knights AC, Williams ER, Bond IP (2008) Biomimetic reliability strategies for self-healing vascular networks in engineering materials. J R Soc Interface 5:735–747
22. Williams HR, Trask RS, Weaver P, Bond IP (2008) Minimum mass vascular networks in multifunctional materials. J R Soc Interface 5:55–65
23. Berfield T, Patel H, Shimmin R, Braun P, Lambros J, Sottos N (2006) Fluorescent image correlation for nanoscale deformation measurements. Small 2:631–635
24. Berfield TA, Patel JK, Shimmin RG, Braun PV, Lambros J, Sottos NR (2007) Micro- and nanoscale deformation measurement of surface and internal planes via digital image correlation. Exp Mech 47:51–62

25. Bruck H, McNeill S, Sutton M, Peters W (1989) Digital image correlation using newton-raphson method of partial-differential correction. Exp Mech 29:261–267
26. Peters WH, Ranson WF (1982) Digital imaging techniques in experimental stress-analysis. Opt Eng 21:427–431
27. Verhaegh N, Blaaderen A (1994) Dispersions of rhodamine-labeled silica spheres: synthesis, characterization, and fluorescence confocal scanning microscopy. Langmuir 10: 1427–1438
28. Bornert M, Bremand F, Doumalin P, Dupre JC, Fazzini M, Grediac M, Hild F, Mistou S, Molimard J, Orteu JJ, Robert L, Surrel Y, Vacher P, Wattrisse B (2009) Assessment of digital image correlation measurement errors: methodology and results. Exp Mech 49:353–370
29. Besnard G, Hild F, Roux S (2006) "Finite-element" displacement fields analysis from digital images: application to Portevin–Le Châtelier bands. Exp Mech 46(6):789–803
30. Savin G (1970) Stress distribution around holes. NASA Technical Translation. Washington, D.C.
31. Savin G (1961) Stress concentration around holes. Pergamon Press, New York
32. Ahmed S, Jones F (1990) A review of particulate reinforcement theories for polymer composites. J Mater Sci 25: 4933–4942